Research Article

ADVANCED PHOTONICS

Dynamic photonic barcodes for molecular detection based on cavity-enhanced energy transfer

Yunke Zhou,[a,†] Zhiyi Yuan,[a,†] Xuerui Gong,[a] Muhammad D. Birowosuto,[a,b] Cuong Dang,[a] and Yu-Cheng Chen[a,c,*]

[a]Nanyang Technological University, School of Electrical and Electronic Engineering, Singapore
[b]CINTRA UMI CNRS/NTU/THALES, Singapore
[c]Nanyang Technological University, School of Chemical and Biomedical Engineering, Singapore

Abstract. Optical barcodes have demonstrated a great potential in multiplexed bioassays and cell tracking for their distinctive spectral fingerprints. The vast majority of optical barcodes were designed to identify a specific target by fluorescence emission spectra, without being able to characterize dynamic changes in response to analytes through time. To overcome these limitations, the concept of the bioresponsive dynamic photonic barcode was proposed by exploiting interfacial energy transfer between a microdroplet cavity and binding molecules. Whispering-gallery modes resulting from cavity-enhanced energy transfer were therefore converted into photonic barcodes to identify binding activities, in which more than trillions of distinctive barcodes could be generated by a single droplet. Dynamic spectral barcoding was achieved by a significant improvement in terms of signal-to-noise ratio upon binding to target molecules. Theoretical studies and experiments were conducted to elucidate the effect of different cavity sizes and analyte concentrations. Time-resolved fluorescence lifetime was implemented to investigate the role of radiative and non-radiative energy transfer. Finally, microdroplet photonic barcodes were employed in biodetection to exhibit great potential in fulfilling biomedical applications.

Keywords: whispering-gallery modes; optical barcodes; fluorescence resonance energy transfer; molecular sensing; biointerface; cavity-enhancement.

Received Aug. 9, 2020; revised manuscript received Sep. 28, 2020; accepted for publication Oct. 2, 2020; published online Oct. 28, 2020.

[DOI: 10.1117/1.AP.2.6.066002]

1 Introduction

Microcavities have emerged as a promising tool, attracting widespread attention for its potential to enhance light–matter interactions in biomedical and biological applications.[1–6] Various types of resonators have been exploited over the past decade, such as Fabry–Pérot microcavities,[7–10] whispering-gallery mode (WGM) resonators,[11–17] and photonic crystals.[18,19] Notably, WGM microcavities possess remarkably high quality factor (Q-factor) and small mode volume, where the spectrum with a series of sharp peaks originates from cavity modulation.[1–3,11,12,20] Consequently, WGM offers an innovative system of spectroscopic encoding for plenty of applications.[21–25] Recently, micro/nano photonic barcodes have been widely applied in multiplexed bioassays,[24,26–28] cell tagging,[29,30] encoding,[31] anti-counterfeiting, and information security.[21,25,32,33] In general, the concept of optical barcodes usually refers to a fixed spectral pattern corresponding to a single target. However, the ability to monitor dynamic changes of optical barcodes remains challenging.

The vast majority of WGM resonators reported to-date are classified as passive resonators; they require evanescent wave coupling and operate based on changes of the modes induced by perturbations occurring inside the evanescent light fields.[3,6] In contrast, active resonators that utilize analytes as a gain medium can support free space excitation and collection to acquire more biological information from emission signals.[8] Modulated fluorescence (MFL) refers to the fluorescence

*Address all correspondence to Yu-Cheng Chen, yucchen@ntu.edu.sg
†These authors contributed equally.

emission modulated by resonators, in which enhanced spontaneous emission at resonant modes is introduced by the Purcell effect.[1,34–37] When considering molecular detection, the mode occupation factor[38] of the analyte outside the cavity is only a few tenths of that inside the cavity (see Fig. S1 in the Supplementary Material), leading to reduced effective Q-factor and Purcell factor and unsatisfactory signal-to-noise ratio (SNR). Hence, we introduce resonant energy transfer by separating donors and acceptors at the cavity interface, where radiative fluorescence energy transfer plays a dominant role, as compared to non-radiative Förster resonance energy transfer (FRET). In conventional cases, FRET is a non-radiation mechanism interpreting energy transfer from excited-state donor to ground-state acceptor through resonant dipole–dipole interaction. Unlike FRET, radiative energy transfer is accompanied by electromagnetic radiation and thereby can occur even if the donor and acceptor are far apart, as shown in Fig. 1(a). In the presence of both energy transfer mechanisms, efficient energy transfer and coupling between donors and acceptors (light–matter interaction) may lead to enhanced SNR and detection limits. Taking advantage of the light-harvesting effect, the high concentration of dye (donor) inside the microdroplet triggers cavity-enhanced energy transfer to excite the molecules (acceptor) attached to the cavity interface. The number of binding molecules therefore alters the amount of energy transfer between donor–acceptor, resulting in distinctive MFL emission peaks.

In this study, we propose the concept of a dynamic photonic barcode based on cavity energy transfer and subsequently employ it in molecular detection using a microdroplet. A new encoding rule that focuses on energy density was established for converting the WGM spectra into photonic barcodes (Fig. 1). Time-resolved fluorescence lifetime measurements were also implemented to investigate the role of FRET and its role in cavity energy transfer [Fig. 1(b)]. Dynamic spectral barcoding was achieved by a significant improvement in terms of SNR upon binding to target molecules. The contribution of cavity size and donor/acceptor concentration ratio to cavity energy transfer was investigated through theoretical simulations and experiments. In contrast to laser emission–based detection (where a threshold was required),[12] the achievable detection limit could be lower (nanomolar level). Lastly, potential biosensing applications with streptavidin–biotin conjugates were demonstrated.

2 Experiment

Details of the materials are provided here: Coumarin 6 (Sigma-Aldrich #442631), Rhodamine 6G (Sigma-Aldrich #83697), Rhodamine B (Tokyo Chemical Industry #A5102), BODIPY-R6G (Sigma-Aldrich #795526), Atto 550 NHS ester (Sigma-Aldrich #92835), and Streptavidin (Sigma-Aldrich #S4762) were used as the biochemical reagents in this work. Phosphate-buffered saline (PBS) (Sigma-Aldrich #P4417) and sodium dodecyl sulfate (SDS) (Sigma-Aldrich #L3771) were used for the buffer solution and surfactant. Poly-L-lysine (PLL) (Sigma-Aldrich #P4832) solution (0.01%) was used for electrostatically mounting liquid crystal droplets. All of the microdroplets in this work were prepared using nematic liquid crystal (NLC), in which 4′-pentyl-4-biphenylcarbonitrile (5CB) was purchased from Sigma-Aldrich (#328510) as the NLC material. For the preparation of dye-doped liquid crystals (LCs), 1.75 mg Coumarin 6 powder or 3.8 mg BODIPY-R6G powder was added to 500 μL 5CB LC solvent and stirred on a vortex mixer for 5 min. Different concentrations of dye-doped LCs were subsequently obtained by dilution with pure 5CB LC. For preparing the NLC microdroplet, 10 μL dye-doped LCs were added to 1 mL SDS/PBS surfactant solution and mixed for 5 min on the vortex mixer.

For the preparation of the streptavidin-coated poly(L-lysine) microdroplet, 10 μL BODIPY-R6G-doped liquid crystal was added into 1 mL SDS/PBS solution and sonicated for 5 min. After centrifugation at 5000 rpm for 4 min, the supernatant was replaced with a 0.01% PLL solution and incubated at room temperature for 30 min. The resulted PLL-modified LC microdroplets were washed by adding PBS solution to remove excessive PLL. Then, 0.1 mg/mL streptavidin (SA) solution was added to the PLL-modified LC microdroplets and slowly mixed for 1 h. Finally, the microdroplets were washed with PBS solution twice to remove the unbound SA before biosensing.[39,40] For cavity energy transfer experiments, Rhodamine 6G (mediator) and Rhodamine B (acceptor) solutions were prepared by mixing 20 μM Rhodamine 6G with 20 μM Rhodamine B solution in equal volumes.

A typical upright microscopic system (Nikon NI-E) with a 50×0.6 NA objective was used to excite the sample and collect the WGM emission from the microdroplets. Light from a SOLA light engine was passed through a filter cube to obtain blue excitation light. The excitation wavelength was 430 to 490 nm, with an average light intensity of 2 W/m^2 for all measurements in this study. All of the WGM emission spectra were collected through a high-resolution spectrometer (Andor Kymera 328i/Newton 970). All of the fluorescence images were captured by a ToupTek charge-coupled device (CCD) camera.

3 Results

3.1 Concept of Photonic Barcode via Cavity Energy Transfer

Figure 1(a) illustrates the interaction between donor molecules and acceptor molecules with (bottom) and without (top) a cavity under different molecular distances. The top row shows that nonradiative FRET occurs when donor and acceptor molecules are extremely close (≤ 7 nm). However, when the molecular distances become larger, only weak radiative energy transfer can be sustained between donor and acceptor molecules in free space. Another scenario is when a cavity interface is formed between the donor and acceptor molecules [bottom of Fig. 1(a)]; the photonic environment becomes inhomogeneous due to the cavity modified density of photonic modes. Excited photons from donor molecules tend to be confined into resonant modes, thus energy transfer will mostly exist at the cavity interface where resonances are located (Fig. S1 in the Supplementary Material). As such, acceptor molecules could still be strongly excited even at a relatively larger distance ($\gg 7$ nm). In Fig. 1(b), we provide the time-resolved fluorescence lifetime of donor-droplets and compare them under different acceptor concentrations. The lifetime of the donor (Coumarin 6) was measured to be $\tau_d = 2.42$ ns. Upon adding 1 μM acceptor molecules to the interface, the lifetime of donor–acceptor becomes $\tau_{da} = 2.35$ ns (FRET efficiency $\sim$3%). At a higher acceptor concentration (5 μM), the lifetime of donor–acceptor becomes $\tau_{da} = 1.78$ ns (FRET efficiency $\sim$26%). In both cases, the FRET efficiencies are considered extremely low. The reasons for such low FRET efficiency can be attributed to two reasons. First is the extremely low acceptor/donor concentration ratio at

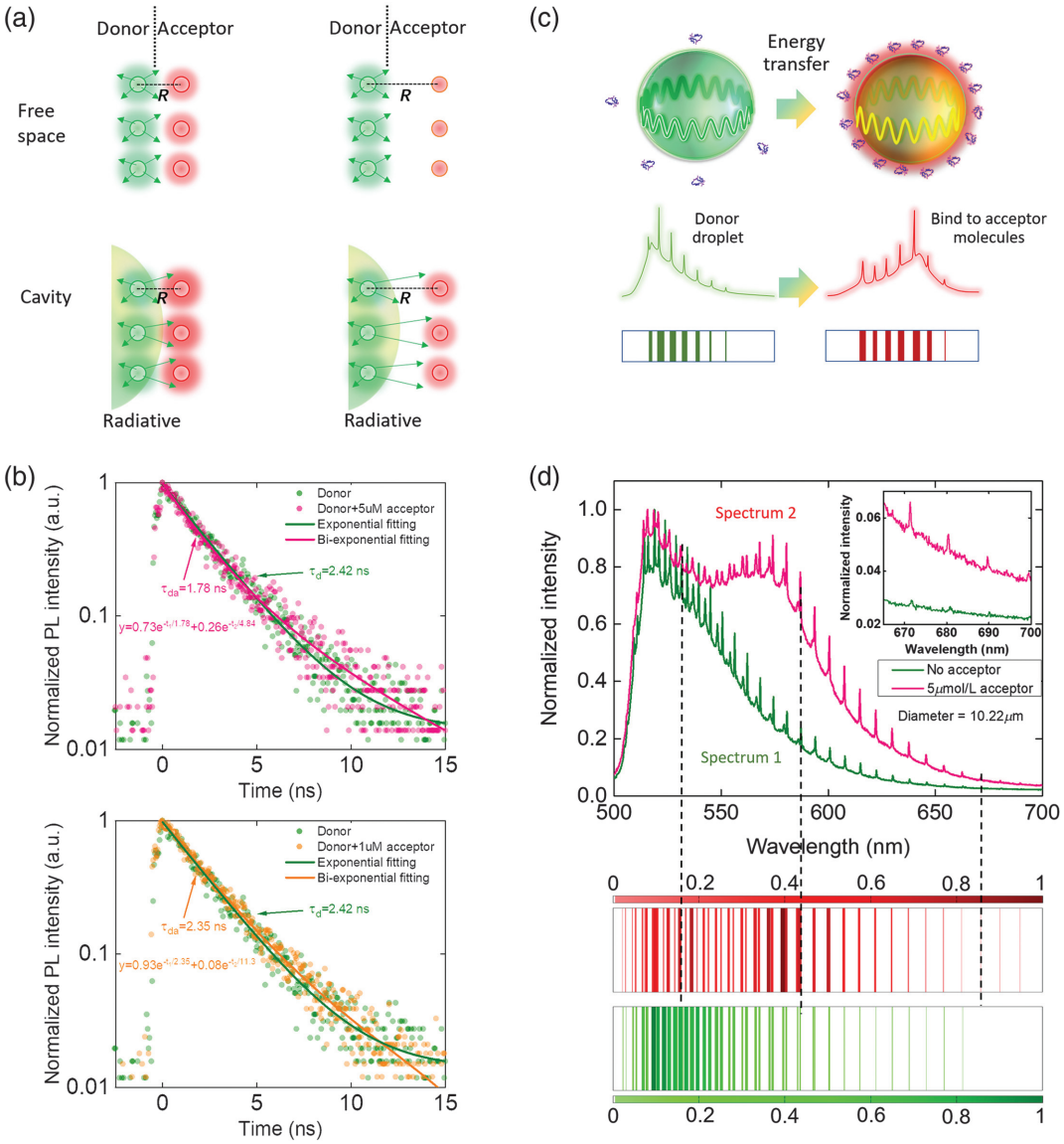

Fig. 1 (a) Comparison of nonradiative FRET and radiative energy transfer, with and without the cavity effect. Left panel: the distance (R) between donor and acceptor molecules is less than 6 nm. Right panel: the distance (R) between donor and acceptor molecules is far apart in free space. Red dots represent acceptor molecules; green dots represent donor molecules. (b) Time-resolved fluorescence lifetime measurement of Coumarin 6 (donor inside, 0.1 mM) microdroplet before (olive dots) and after adding 5 μM (top panel) or 1 μM (bottom panel) Rhodamine molecules (acceptor). When the acceptor concentration increases, the lifetime of the donor becomes faster. The FRET efficiency is around 26% and 3%, respectively. The solid curves were fitted by the scattered dots according to the exponential decay functions. (c) Schematic diagram interpreting cavity energy transfer and the photonic barcoding. The top panel illustrates WGM with and without the acceptor near the cavity boundary. The bottom panel shows the corresponding spectra and photonic barcodes before and after energy transfer. (d) A typical WGM-modulated fluorescent spectrum recorded from a Coumarin 6 donor-droplet (spectrum 1) before and after applying Rhodamine (spectrum 2). The excitation LED wavelength: 430 to 490 nm. The converted barcodes are plotted below. Droplet diameter $=$ 10.22 μm; donor molarity $=$ 0.1 mM; and acceptor molarity $=$ 5 μM.

the interface. Second, only the donor–acceptor molecules near the droplet interface will contribute to the FRET process (see Fig. S2 in the Supplementary Material). Therefore, our findings indicate that strong radiative energy transfer that takes place in the evanescent field region is much more dominant than nonradiative FRET process.

Based on the physical mechanism in Fig. 1(a), the conceptualization of the dynamic photonic barcode was developed

based on cavity energy transfer, as illustrated in Fig. 1(c). We adopted free-space coupling to excite the gain medium within the microcavity and collected the photoluminescence spectrum from the leaky modes and non-directional emissions emitted from the non-resonant region, as shown in Fig. S2 in the Supplementary Material. Energy transfer occurs at the interface of the microcavity, where donor and acceptor are separated, leading to a change in the PL spectrum as well as the optical barcode. Each solid bar is predefined at the center wavelength of the corresponding resonance mode, where the width is determined by its integration of resonance intensity after subtracting the associated fluorescence background. To facilitate the quantification of energy transfer, we correlated the energy integration with a colormap, where the darker color represents a larger spectral integrated intensity (from 0.1 to 1.0).

As a proof-of-concept, Coumarin 6 (C6) and Rhodamine B were selected as the donor–acceptor pairs, respectively. To optimize the energy transfer efficiency, a mediator (Rhodamine 6G) was used (Fig. S3 in the Supplementary Material). Figure 1(d) presents a typical MFL spectrum with quasi-periodic WGM peaks embedded in the fluorescence emission background (spectrum 1, only donor). In the presence of the microcavity, both spontaneous emission rate and photon directivity of the gain medium would be anisotropic, owing to the inhomogeneous local density of states, which is known as a cavity quantum electrodynamic phenomenon called the Purcell effect. The enhancement of the spontaneous emission rate could be expressed by the Purcell factor,[36]

$$F_P = \frac{3}{4\pi^2}\left(\frac{\lambda_{\text{free}}}{n}\right)^3\left(\frac{Q}{V}\right), \tag{1}$$

where λ_{free} is the wavelength in the vacuum, n is the refractive index of the liquid crystal cavity, and Q and V represent the quality factor and mode volume of resonant modes of the cavity, respectively. As such, the sharp peaks result from the edge of the cavity where the modes are located, while the rest of the emission from the gain medium contributes to the fluorescence background (Fig. S2 in the Supplementary Material). However, in the presence of acceptor molecules adhered to the droplet cavity surface by physical absorption (spectrum 2), the WGM peaks beyond 570 nm are evidently enhanced under the same light-emitting diode (LED) pump, indicating that energy has been transferred from the donor band to the acceptor band via cavity energy transfer. The strongest bandwidth of MFL also shifts from 520 to 580 nm, in which several new peaks arise between 670 and 700 nm in the inset of Fig. 1(d).

3.2 Physics of Cavity-Enhanced Energy Transfer

For more comprehensive insights into cavity energy transfer, we applied rate equations to simulate the intensity for every single mode and thereby obtain the efficiency of cavity energy transfer. Equations (2)–(5) describe the dynamics of excited-state molecule density and photon density of the donor and acceptor. The first term in Eqs. (2) and (4) represents direct excitation by the pump source. The second and third terms in Eq. (4) are derived from non-radiative FRET and radiative energy transfer from donor to acceptor, respectively. In Eqs. (2) and (4), the integral terms $\kappa_{\text{rad},D} n_D(t) \int_0^\infty F_{p,D}(\omega) L_D(\omega) \mathrm{d}\omega$ and $\kappa_{\text{rad},} n_A(t) \int_0^\infty F_{p,A}(\omega) L_A(\omega) \mathrm{d}\omega$ represent spontaneous emission in an inhomogeneous photonic environment according to Fermi's golden rule.[36,37] Detailed calculations of the spontaneous emission rate in a microcavity are all provided in the Supplementary Material.

$$\begin{aligned}\frac{\mathrm{d}n_D(t)}{\mathrm{d}t} &= \sigma_{\text{abs},D}(\omega) I_{ph}(t,\omega)[N_{D0} - n_D(t)] - \kappa_F n_D(t) \\ &\quad - \kappa_{\text{rad},D} n_D(t) \int_0^\infty F_{p,D}(\omega) L_D(\omega) \mathrm{d}\omega - \kappa_{n\text{rad},D} n_D(t) \\ &\quad + \frac{c}{\eta_1}[N_{D0} - n_D(t)] \int_0^\infty \sigma_{\text{abs},D}(\omega) q_D(\omega,t) \mathrm{d}\omega,\end{aligned} \tag{2}$$

$$\begin{aligned}\frac{\mathrm{d}q_D(\omega,t)}{\mathrm{d}t} &= \kappa_{\text{rad},D} n_D(t) F_{p,D}(\omega) L_D(\omega) \\ &\quad - \frac{c}{\eta_2}\sigma_{\text{abs},A}(\omega) q_D(\omega,t)[N_{A0} - n_A(t)] \\ &\quad - \frac{c}{\eta_1}[N_{D0} - n_D(t)]\sigma_{\text{abs},D}(\omega) q_D(\omega,t) - \frac{q_D(\omega,t)}{\tau_{c,D}(\omega)},\end{aligned} \tag{3}$$

$$\begin{aligned}\frac{\mathrm{d}n_A(t)}{\mathrm{d}t} &= \sigma_{\text{abs},A}(\omega) I_{ph}(t,\omega)[N_{A0} - n_A(t)] + \kappa_F n_D(t) \\ &\quad + \frac{c}{\eta_2}[N_{A0} - n_A(t)] \int_0^\infty \sigma_{\text{abs},A}(\omega) q_D(\omega,t) \mathrm{d}\omega \\ &\quad + \frac{c}{\eta_2}[N_{A0} - n_A(t)] \int_0^\infty \sigma_{\text{abs},A}(\omega) q_A(\omega,t) \mathrm{d}\omega \\ &\quad - \kappa_{\text{rad},A} n_A(t) \int_0^\infty F_{p,A}(\omega) L_A(\omega) \mathrm{d}\omega - \kappa_{n\text{rad},A} n_A(t),\end{aligned} \tag{4}$$

$$\begin{aligned}\frac{\mathrm{d}q_A(\omega,t)}{\mathrm{d}t} &= \kappa_{\text{rad},A} n_A(t) F_{p,A}(\omega) L_A(\omega) \\ &\quad - \frac{c}{\eta_2}[N_{A0} - n_A(t)]\sigma_{\text{abs},A}(\omega) q_A(\omega,t) - \frac{q_A(\omega,t)}{\tau_{c,A}(\omega)}.\end{aligned} \tag{5}$$

In the above equations, $n_D(t)$, $n_A(t)$, $q_D(\omega,t)$, and $q_A(\omega,t)$ represent the densities of donor and acceptor molecules in the excited state and densities of the photon at frequency ω emitted by the donor and acceptor molecules, respectively. $\sigma_{\text{abs},D}(\omega)$ and $\sigma_{\text{abs},A}(\omega)$ are the absorption cross-sections of the donor and acceptor at frequency ω, respectively. $I_{ph}(t,\omega)$ is the time-dependent pump at the frequency ω in units of photons/$(\text{cm}^2 \cdot \text{s})$. N_{D0} and N_{A0} are the total concentration of donor and acceptor molecules, respectively. η_1 and η_2 represent the refractive index of the microcavity and the surrounding medium, respectively. κ_F is the FRET rate, and $\kappa_{\text{rad},D}$, $\kappa_{n\text{rad},D}$, $\kappa_{\text{rad},A}$, and $\kappa_{n\text{rad},A}$ denote radiative decay rate and nonradiative decay rate of the donor and acceptor, respectively. $F_{p,D}(\omega)$ and $F_{p,A}(\omega)$, respectively, are the Purcell factor of the donor and acceptor at frequency ω. $L_D(\omega)$ and $L_A(\omega)$ represent the spontaneous emission line shape of the donor and acceptor, respectively. $\tau_{c,D}(\omega)$ and $\tau_{c,A}(\omega)$ are the photon lifetime of the donor emission and acceptor emission, respectively, at frequency ω.

To further demonstrate the significance of cavity energy transfer, we compared the WGM spectra with and without the donor inside a microdroplet cavity in Figs. 2(a) and 2(b), respectively. Figure 2(a) shows the dynamic MFL spectra of a Coumarin 6 (C6, donor) microdroplet upon adding 5 μM Rhodamine molecule (acceptor). Over time, the increased amount of acceptor molecules continuously binds to the surface of the microdroplet due to gradient diffusion, as shown in the time-dependent fluorescence image (inset). According to the dynamic spectra, the energy distribution of the MFL tends to redshift due to the increase in energy transfer efficiency. The corresponding photonic barcodes are provided in the right panel, where one can clearly observe the process of energy transfer. As a comparison, Fig. 2(b) presents the modulated emission spectra of a pure LC microdroplet upon adding 5 μM Rhodamine. Slight WGM modulation of fluorescence emission can be observed in Fig. 2(b), where the corresponding photonic barcodes are plotted on the right panel. Without donor excitation from the droplet, the wavelength remains the same in the photonic barcodes. Given that both results in Figs. 2(a) and 2(b) show that external acceptors can be involved in cavity resonance through the evanescent coupling, Fig. 2(a) presented a much higher SNR and dynamic range. More significantly, the number of optical barcodes that could be generated with the existence of donor excitation is estimated to be 10^9 times more complex than that without a donor (details can be found in the Supplementary Material). In addition, the establishment of equilibrium for a transparent droplet was simulated under a green-LED pump (suitable for acceptors and equivalent to excitation from the donor) in Fig. S4 in the Supplementary Material. The density of excited states of the acceptor in equilibrium in the absence of donor was found to be 8 times less than that with the donor, implying that the WGM emission from Rhodamine is supposed to be 8 times different as well.

Note that since Rhodamine molecules will continue to bind on the droplet surface [in Fig. 2(a)], it is expected that the WGM spectrum will continue to change until it reaches an equilibrium. As shown in Fig. 2(c), we demonstrate that the WGM spectra and converted barcodes will reach an equilibrium after 130 s, which could possibly be used to determine the concentration. In particular, we specifically chose three different peaks extracted from Fig. 2(c) and traced the energy transfer efficiency over 7 min in Fig. 2(d). The energy transfer efficiency was calculated by $E = 1 - I_{DA}/I_D$, where I_D and I_{DA} represent the intensity of the mode in the absence and presence of the acceptor, respectively. Obviously, the peak wavelengths become stabilized eventually; hence, we believe that the barcodes can read out repeatedly after detailed calibrations.

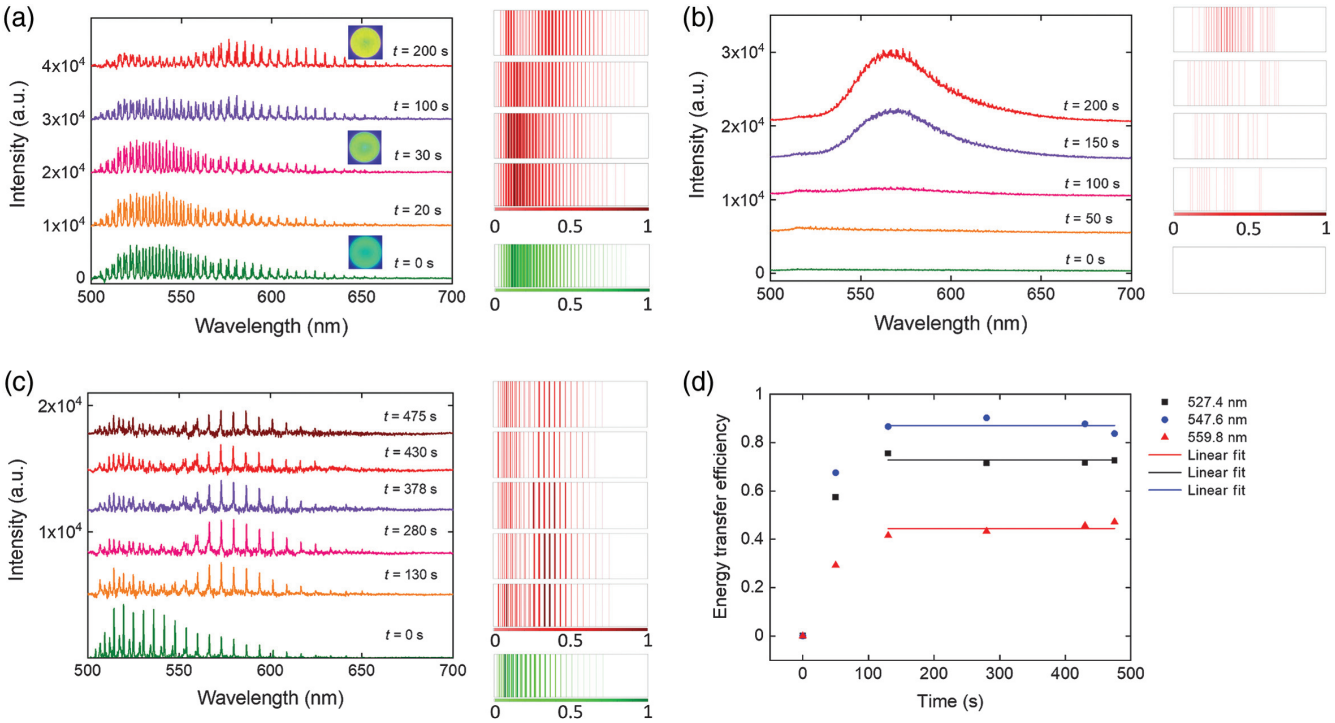

Fig. 2 (a) and (b) Comparison between WGM emission spectra obtained from (a) Coumarin 6 microdroplet (with the donor in the cavity) and (b) pure microdroplet (without donor in the cavity) after adding 5 μM Rhodamine (acceptor molecules). Different colors of spectra denote the time at which the spectrum was collected. The converted dynamic barcodes for respective time periods are plotted in the right panel for both cases under the same rule. The inset CCD images in (a) show the WGM MFL emission changes as the acceptor concentrations increase through time (the same droplet). Droplet diameter = 12 μm; donor molarity = 0.1 mM; and excitation LED wavelength: 430 to 490 nm. (c) Dynamic spectra of a Coumarin 6 microdroplet after adding 5 μM Rhodamine from $t = 0$ to 475 s. (d) Calculated energy transfer efficiency from (c) at different peaks: 527.4 nm (black dots), 547.6 nm (blue dots), and 559.8 nm (red dots) as a function of time. The solid line is fitted according to the data after 130 s.

3.3 Investigation of the Cavity Size and Molecular Concentration

Here, we explore the minimum cavity size that can support MFL and cavity energy transfer. Figures 3(a)–3(c) demonstrate the MFL spectra of Coumarin 6 droplets with different sizes before and after adding 5 μM acceptor solution. The insets represent the fluorescence image captured by a monochromatic CCD (pseudocolor), illustrating the diameter of each droplet. The free spectral range (FSR) agrees well with the droplet diameter in each figure, as shown in the inset. For instance, in Fig. 3(a), the corresponding eigenmodes of each resonance peak were numerically solved and fitted with a diameter of 3.52 μm. As the cavity size increases, the number of resonance modes, as well as the emission intensity, increases due to the multimode nature of WGM (Fig. S5 in the Supplementary Material). For larger droplets, higher-order TM modes ($s = 2$, TM_l^2) also participate in the cavity energy transfer due to the significant evanescent field outside the cavity [see Figs. S1(b) and S1(d) in the Supplementary Material]. The changes of spectra through barcodes with multimodes become complex and distinguishable. Note that the blueshift shown in Fig. 3(a) is due to the temperature effect under LED excitation. Since the ambient temperature will affect the refractive index (RI) of liquid crystals, a blueshift for TM and redshift for TE is sometimes expected regardless of droplet size.[41]

Theoretical simulation outcomes are also in good agreement with the experimental results. As presented in the simulation (Fig. S6 in the Supplementary Material), larger droplets generated a more significant intensity change than smaller droplets under a concentration of 5 μM. Nonetheless, in the experiment, it is noteworthy that large droplets suffer from sensitivity when the acceptor concentration is relatively low (nM level). At lower acceptor concentrations, the acceptor signals will be immersed by the strong donor emission from larger droplets. In this case, a smaller cavity size shall be more effective to the binding events due to a larger surface-to-volume ratio. The occupation factor of the evanescent field increases as the cavity size decreases, therefore the ratio of Purcell factors $F_{p,A}(\omega)/F_{p,D}(\omega)$ becomes closer to 1.

Next, we investigated the effect of different acceptor concentrations (0.5, 1, 2.5, and 5 μM) under similar-sized droplets in Figs. 4(a)–4(d). By extracting the WGM emission spectra from Figs. 4(a)–4(d), the converted photonic barcodes after binding to different acceptor concentrations were plotted, respectively [see Fig. 4(e)]. As the concentration of acceptors increased, the relative intensity of peaks at longer wavelengths increased significantly, implying an increased efficiency of cavity energy transfer. The simulation result also agrees well with this phenomenon (Fig. S7 in the Supplementary Material).

3.4 Proof-of-Concept for Biomolecular Detection

Finally, we demonstrated the potential application of cavity energy transfer by choosing streptavidin–biotin conjugates as the target molecules. As shown in Fig. 5(a), a streptavidin (SA)-coated dye-doped droplet was used as the donor, while biotin molecules labeled with Atto 550 (Biotin-Atto 550) were employed as the target acceptor. Details of droplet modification and coating are provided in Sec. 2. Note that BODIPY-R6G was selected as the donor dye, owing to its huge spectral overlap with Atto 550 [Fig. 5(b)]. Figure 5(c) presents the WGM spectra when Biotin-Atto 550 molecules were applied to the donor droplet. Significant changes can also be observed via the optical barcode, as shown in the bottom panel of Fig. 5(c), where cavity energy transfer between BODIPY-R6G and Atto 550 occurred. As shown in the inset, new modes TM_{59}^l, TM_{60}^l, and TM_{61}^l were

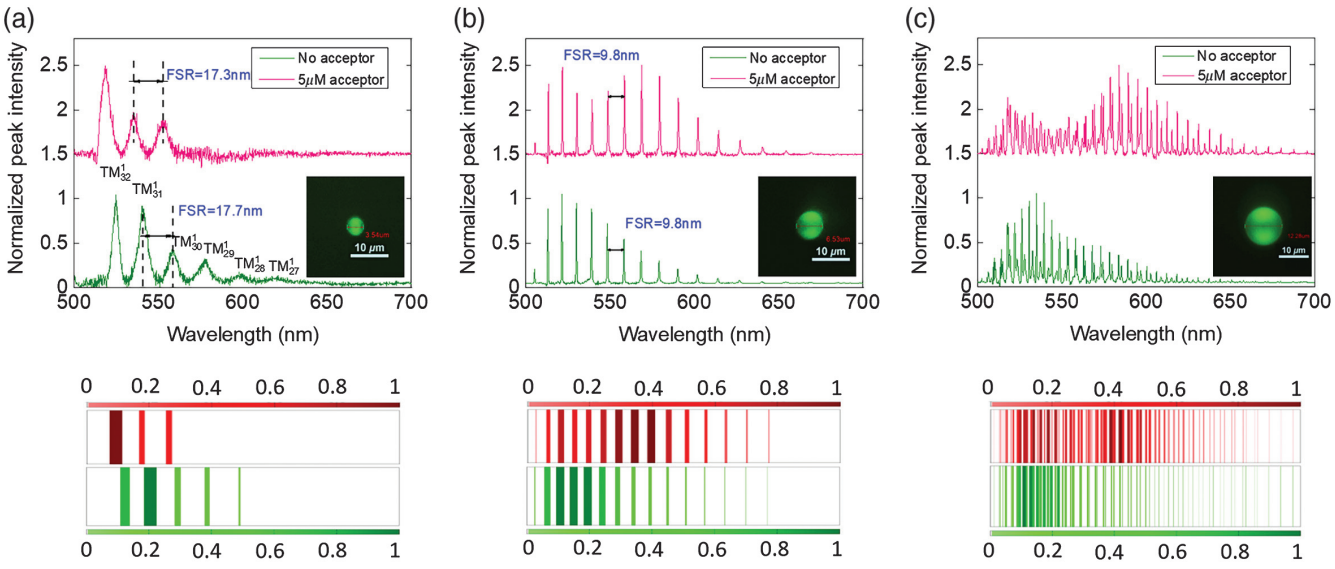

Fig. 3 MFL spectra and the corresponding photonic barcodes under different cavity diameters of (a) 3.54, (b) 6.53, or (c) 12.28 μm. All of the green curves (barcodes) represent Coumarin 6 droplets before binding to any acceptor molecules. All of the red curves (barcode) represent Coumarin 6 droplets after adding 5 μM Rhodamine molecules. The insets show the fluorescence images captured by a monochromatic CCD (pseudocolor). All scale bars represent 10 μm. In particular, TM_l^s modes were calculated according to the characteristic equation (see Supplementary Material). The excitation LED wavelength: 430 to 490 nm and donor molarity = 0.1 mM.

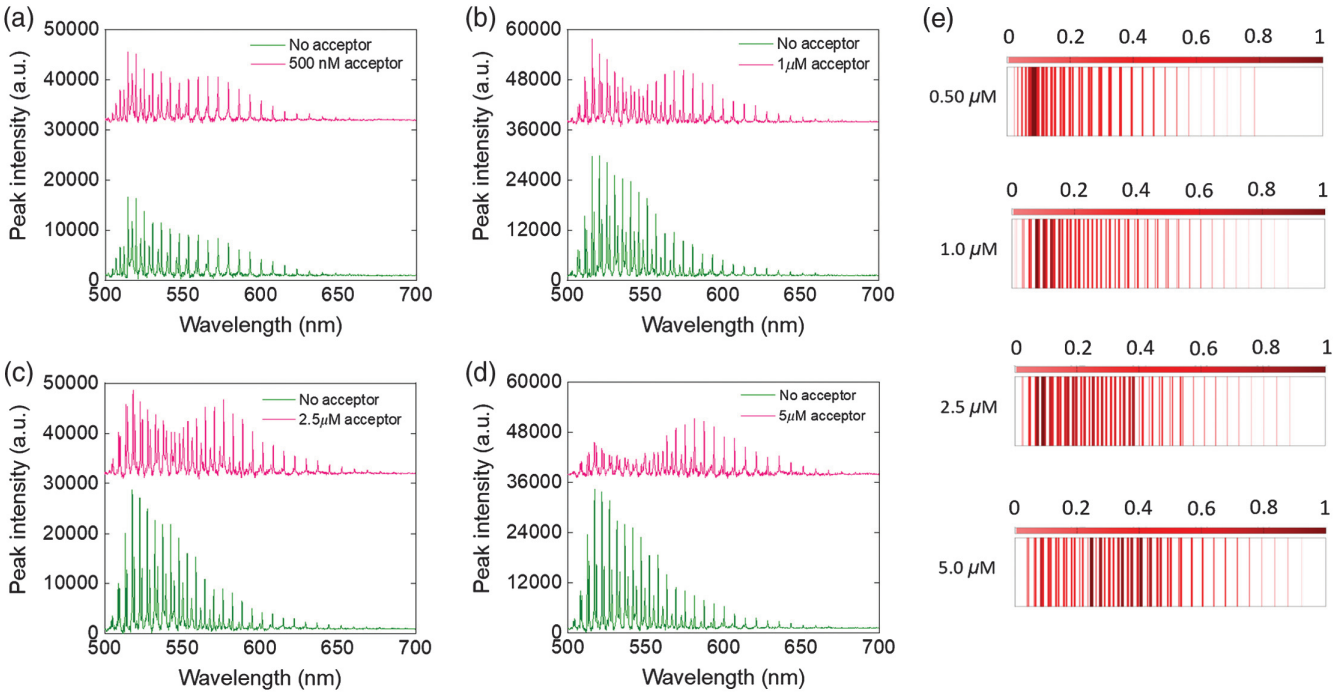

Fig. 4 (a)–(d) Equilibrium WGM spectra of Coumarin 6 microdroplets before (green curve) and after (pink curve) adding (a) 500 nM, (b) 1 μM, (c) 2.5 μM, and (d) 5 μM Rhodamine molecule solution. All WGM spectra were measured after reaching equilibrium under the same excitation wavelength (430 to 490 nm) and excitation energy. The fluorescence background was subtracted for clarity. (e) Photonic barcodes resulted from different Rhodamine concentrations [converted from the WGM spectra from (a)–(d)].

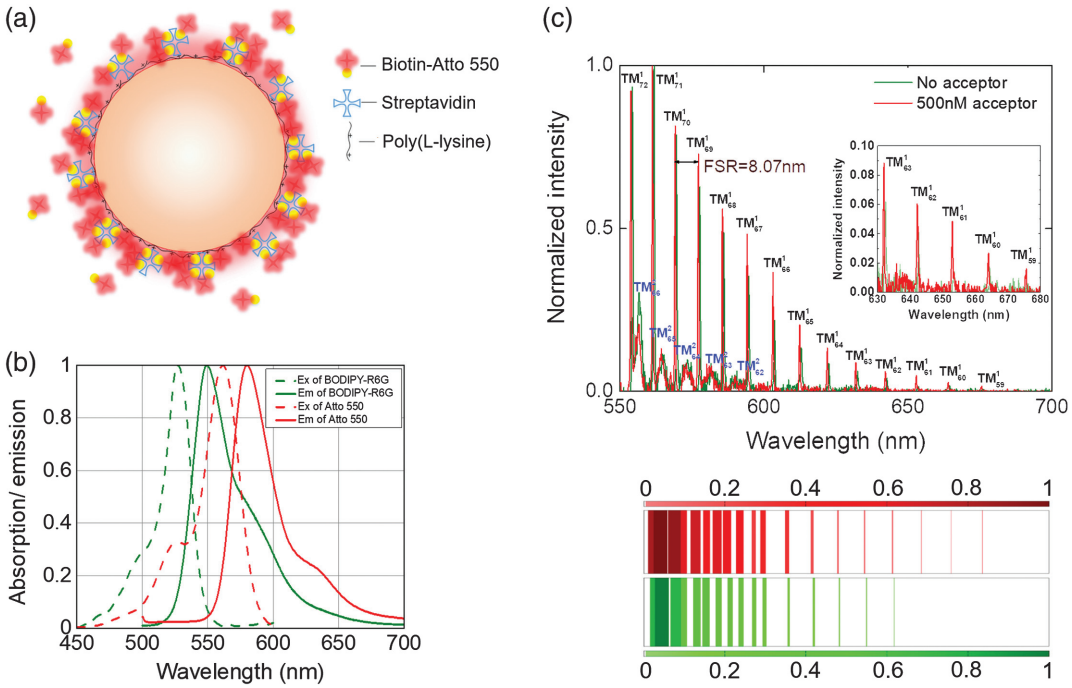

Fig. 5 (a) Schematic illustration of the Biotin-Atto 550 molecules binding to SA-coated microdroplet. (b) Normalized excitation (dashed line) and emission (solid line) spectra of BODIPY-R6G (green) and Atto 550 (red). (c) Comparison of the WGM spectra before and after adding 500 nM Biotin-Atto 550. The inset shows details of the spectral line. The corresponding photonic barcodes are plotted below. Excitation wavelength: 430 to 490 nm; droplet diameter = 8.17 μm; and BODIPY-R6G (donor) concentration = 0.1 mM. The fluorescence background was subtracted for clarity.

generated after specific binding to Biotin-Atto 550, demonstrating the potential for utilizing cavity energy transfer in biosensing technology.

4 Conclusions

In this study, we have reported a concept of dynamic photonic barcodes based on cavity energy transfer, and subsequently employed it in molecular detection. By separating the donor and acceptor at the cavity interface, cavity-enhanced energy transfer was observed between the microcavity and binding molecules. When biomolecules bind to the cavity interface, the MFL spectra shift from green emission to longer wavelengths. An encoding rule was therefore developed to identify the changes of the WGM MFL emission spectra, where more than 10^9 distinctive barcodes could be generated. Different droplet sizes and molecular concentrations were also investigated theoretically and experimentally. Finally, a simple proof-of-concept for biomolecular detection was demonstrated using dynamic photonic barcodes. We envisage that the proposed concept in this study can be widely applied in many biosensing applications and optical encryption. To improve the detection limit, it may be possible to improve the Q-factor of the droplet material or to increase the overlap region between selection of the donor–acceptor pair spectrum. This study aims to focus on the physical concept and show the possibility of using this as a more distinguishable readout. Multiplexed detection can be easily achieved by choosing multiple dye-doped droplets (donor) and fluorophores (acceptor). With the addition of one fluorophore (donor or acceptor), the total number of optical barcodes could increase dramatically by several orders. Such complex barcodes could therefore provide a better way to identify and monitor molecular interactions in real time.

Acknowledgments

We would like to thank the Centre of Bio-Devices and Bioinformatics and CNRS International—Nanyang Technological University-Thales Research Alliance (CINTRA) for lab support. We would also like to thank NTU for the startup grant (SUG - M4082308.040).

References

1. K. J. Vahala, "Optical microcavities," *Nature* **424**, 839–846 (2003).
2. Y. C. Chen and X. Fan, "Biological lasers for biomedical applications," *Adv. Opt. Mater.* **7**(17), 1900377 (2019).
3. T. Reynolds et al., "Fluorescent and lasing whispering gallery mode microresonators for sensing applications," *Laser Photonics Rev.* **11**(2), 1600265 (2017).
4. X. Fan and S. H. Yun, "The potential of optofluidic biolasers," *Nat. Methods* **11**(2), 141–147 (2014).
5. A. Fernandez-Bravo et al., "Continuous-wave upconverting nanoparticle microlasers," *Nat. Nanotechnol.* **13**(7), 572–577 (2018).
6. E. Kim, M. D. Baaske, and F. Vollmer, "Towards next-generation label-free biosensors: recent advances in whispering gallery mode sensors," *Lab Chip* **17**(7), 1190–1205 (2017).
7. Y. C. Chen et al., "Versatile tissue lasers based on high-Q Fabry–Perot microcavities," *Lab Chip* **17**(3), 538–548 (2017).
8. Y. C. Chen et al., "Laser-emission imaging of nuclear biomarkers for high-contrast cancer screening and immunodiagnosis," *Nat. Biomed. Eng.* **1**, 724–735 (2017).
9. C. Gong et al., "Sensitive sulfide ion detection by optofluidic catalytic laser using horseradish peroxidase (HRP) enzyme," *Biosens. Bioelectron.* **96**, 351–357 (2017).
10. M. Humar, M. C. Gather, and S. H. Yun, "Cellular dye lasers: lasing thresholds and sensing in a planar resonator," *Opt. Express* **23**(21), 27865–27879 (2015).
11. M. Humar et al., "Electrically tunable liquid crystal optical microresonators," *Nat. Photonics* **3**, 595–600 (2009).
12. Z. Yuan et al., "Lasing-encoded microsensor driven by interfacial cavity resonance energy transfer," *Adv. Opt. Mater.* **8**(7), 2070029 (2020).
13. Y. C. Chen, Q. Chen, and X. Fan, "Optofluidic chlorophyll lasers," *Lab. Chip* **16**(12), 2228–2235 (2016).
14. Y. C. Chen, Q. Chen, and X. Fan, "Lasing in blood," *Optica* **3**(8), 809–815 (2016).
15. M. Humar and I. Muševič, "Surfactant sensing based on whispering-gallery-mode lasing in liquid-crystal microdroplets," *Opt. Express* **19**(21), 19836–19844 (2011).
16. M. Humar and S. H. Yun, "Whispering-gallery-mode emission from biological luminescent protein microcavity assemblies," *Optica* **4**(2), 222–228 (2017).
17. V. D. Ta et al., "Microsphere solid-state biolasers," *Adv. Opt. Mater.* **5**(8), 1601022 (2017).
18. S. Hachuda et al., "Selective detection of sub-atto-molar Streptavidin in 10(13)-fold impure sample using photonic crystal nanolaser sensors," *Opt. Express* **21**(10), 12815–12821 (2013).
19. K. Watanabe et al., "Label-free and spectral-analysis-free detection of neuropsychiatric disease biomarkers using an ion-sensitive GaInAsP nanolaser biosensor," *Biosens. Bioelectron.* **117**, 161–167 (2018).
20. N. Martino et al., "Wavelength-encoded laser particles for massively multiplexed cell tagging," *Nat. Photonics* **13**, 720–727 (2019).
21. Z. Gao et al., "Covert photonic barcodes based on light controlled acidichromism in organic dye doped whispering-gallery-mode microdisks," *Adv. Mater.* **29**(30), 1701558 (2017).
22. D. Richter, M. Marincic, and M. Humar, "Optical-resonance-assisted generation of super monodisperse microdroplets and microbeads with nanometer precision," *Lab Chip* **20**(4), 734–740 (2020).
23. F. Ramiro-Manzano et al., "Porous silicon microcavities based photonic barcodes," *Adv. Mater.* **23**(27), 3022–3025 (2011).
24. M. Humar, A. Upadhya, and S. H. Yun, "Spectral reading of optical resonance-encoded cells in microfluidics," *Lab Chip* **17**(16), 2777–2784 (2017).
25. D. Okada et al., "Optical microresonator arrays of fluorescence-switchable diarylethenes with unreplicable spectral fingerprints," *Mater. Horiz.* **7**(7), 1801–1808 (2020).
26. H. H. Gorris and O. S. Wolfbeis, "Photon-upconverting nanoparticles for optical encoding and multiplexing of cells, biomolecules, and microspheres," *Angew. Chem. Int. Ed.* **52**(13), 3584–3600 (2013).
27. H. Lee et al., "Colour-barcoded magnetic microparticles for multiplexed bioassays," *Nat. Mater.* **9**, 745–749 (2010).
28. D. S.-Z. Zhang et al., "Dual-encoded microbeads through a host-guest structure: enormous, flexible, and accurate barcodes for multiplexed assays," *Adv. Funct. Mater.* **26**(34), 6146–6157 (2016).
29. A. H. Fikouras et al., "Non-obstructive intracellular nanolasers," *Nat. Commun.* **9**, 4817 (2018).
30. M. Schubert et al., "Lasing within live cells containing intracellular optical microresonators for barcode-type cell tagging and tracking," *Nano Lett.* **15**(8), 5647–5652 (2015).
31. F. Yesilkoy et al., "Ultrasensitive hyperspectral imaging and biodetection enabled by dielectric metasurfaces," *Nat. Photonics* **13**, 390–396 (2019).
32. Y. Yao et al., "Heteroepitaxial growth of multiblock Ln-MOF microrods for photonic barcodes," *Angew. Chem. Int. Ed.* **58**(39), 13803–13807 (2019).

33. Z. Gao et al., "Spatially responsive multicolor lanthanide-MOF heterostructures for covert photonic barcodes," *Angew. Chem. Int. Ed.* **59**(43), 19060–19064 (2020).
34. A. E. Krasnok et al., "An antenna model for the Purcell effect," *Sci. Rep.* **5**(1), 12956 (2015).
35. E. M. Purcell, H. C. Torrey, and R. V. Pound, "Resonance absorption by nuclear magnetic moments in a solid," *Phys. Rev.* **69**(1–2), 37–38 (1946).
36. B. Romeira and A. Fiore, "Purcell effect in the stimulated and spontaneous emission rates of nanoscale semiconductor lasers," *IEEE J. Quantum Electron.* **54**(2), 2000412 (2018).
37. J. Gérard et al., "Enhanced spontaneous emission by quantum boxes in a monolithic optical microcavity," *Phys. Rev. Lett.* **81**(5), 1110–1113 (1998).
38. H.-J. Moon, Y.-T. Chough, and K. An, "Cylindrical microcavity laser based on the evanescent-wave-coupled gain," *Phys. Rev. Lett.* **85**(15), 3161–3164 (2000).
39. S. Sidiq et al., "Poly(l-lysine)-coated liquid crystal droplets for cell-based sensing applications," *J. Phys. Chem. B* **121**(16), 4247–4256 (2017).
40. I. Verma, S. Sidiq, and S. K. Pal, "Poly(l-lysine)-coated liquid crystal droplets for sensitive detection of DNA and their applications in controlled release of drug molecules," *ACS Omega* **2**(11), 7936–7945 (2017).
41. M. Humar, "Liquid-crystal-droplet optical microcavities," *Liq. Cryst.* **43**(13–15), 1937–1950 (2016).
42. A. N. Oraevsky, "Whispering-gallery waves," *Quantum Electron. (Woodbury)* **32**(5), 377 (2002).
43. J. R. Lakowicz, *Principles of Fluorescence Spectroscopy*, Springer Science & Business Media (2013).

Yunke Zhou is currently a PhD graduate student at Tsinghua University, China. He was a visiting research student at Nanyang Technological University, Singapore, 2019–2020.

Zhiyi Yuan is a PhD graduate student at Nanyang Technological University, Singapore.

Xuerui Gong is a PhD graduate student at Nanyang Technological University, Singapore.

Muhammad D. Birowosuto is currently a visiting fellow and manager at CNRS International—Nanyang Technological University-Thales Research Alliance (CINTRA).

Cuong Dang is an assistant professor at Nanyang Technological University, Singapore. He is also the director for Centre for OptoElectronics and Biophotonics.

Yu-Cheng Chen received a PhD in biomedical engineering from the University of Michigan, Ann Arbor, in 2017 and has worked as an assistant professor at Nanyang Technological University, Singapore since 2018. His research mainly focuses in optofluidics, biolasers, biophotonics, biosensors and imaging, and novel on-chip laser devices.